Acta Crystallographica Section B
Structural Science
ISSN 0108-7681

Structure and microstructure of hexagonal $Ba_3Ti_2RuO_9$ by electron diffraction and microscopy

Christian Maunders,[a,b]* Joanne Etheridge,[a] Natasha Wright[b] and Harold J. Whitfield[a]

[a]School of Physics and Materials Engineering, Building 69, Monash University, Victoria 3800, Australia, and [b]CSIRO Manufacturing and Infrastructure Technology, Private Bag 33, Clayton South MDC, Victoria 3169, Australia

Correspondence e-mail: christian.maunders@spme.monash.edu.au

Received 2 December 2004
Accepted 18 January 2005

We have used electron microscopy and diffraction to refine the structure and investigate the microstructure of $Ba_3Ti_2RuO_9$. The parent compound is hexagonal $BaTiO_3$ with the space group $P6_3/mmc$. Using convergent-beam electron diffraction (CBED) combined with electron-sensitive image plates we have found that the space group of $Ba_3Ti_2RuO_9$ is the non-centrosymmetric group $P6_3mc$ at room temperature and at ~ 110 K. This is consistent with the Ru and Ti atoms occupying alternate face-sharing octahedral sites in the $\langle 0001 \rangle$ direction. This maintains the *c*-glide, but breaks the mirror normal to the *c* axis and consequently removes the centre of symmetry. Using powder X-ray diffraction, we have measured the lattice parameters from polycrystalline samples to be $a = 5.7056 \pm 0.0005$, $c = 14.0093 \pm 0.0015$ Å at room temperature. Using high-resolution electron microscopy (HREM) we observed highly coherent, low-strain $\{10\bar{1}0\}$ grain boundaries intersecting at 60 and 120°. From CBED we deduce that adjacent grains are identical but for the relative phase of the Ti and Ru atom ordering along the *c* axis. HREM also revealed occasional stacking faults, normal to the *c*-axis.

1. Introduction

The perovskite system can accommodate a range of elemental combinations, structural phases and structural distortions. These in turn generate a wealth of electronic and magnetic properties, from ferroelectricity to colossal magnetoresistance, that have been extensively studied and in some cases developed for application in industry, for example, as capacitors, transducers and memory devices.

The hexagonal perovskites have received less attention, in part, because the hexagonal phase often only exists at temperatures much higher than room temperature and so is less accessible to study. The hexagonal perovskites are nevertheless important compounds, many having exotic electronic and/or magnetic properties. In addition, the hexagonal phases place the constituent elements in distinctly different bonding environments to their cubic derived sister phases and as such provide a useful reference structure with which to compare and understand the structure–bonding–property relationships in these compounds, as has been done with great profit by Hill and co-workers (for example, Hill, 2000).

In 1961, Dickson *et al.* (1961) showed that a series of room-temperature stable hexagonal perovskites could be generated from $BaTiO_3$ by partial substitution of the Ti atoms with other transition metal atoms, to give the formula unit $Ba_3Ti_2MO_9$, where M = V, Cr, Mn, Fe, Co, Ru, Rh, Ir or Pt. More recently, Grey *et al.* (1998), Langhammer *et al.* (2000) and Keith *et al.* (2004) have shown that fractional substitution of M = Mg, Al,

Cr, Mn, Fe, Co, Zn, Ga, Ni or In in $Ba(Ti_{1-x}M_x)O_{3-\delta}$, with $0.05 \leq x \leq 0.50$, stabilizes the hexagonal phase. These compounds are potentially important for understanding the phase-transition mechanisms and structure–property relationships, however, in many cases their structures have only been partially determined.

In this paper, we investigate the structure and microstructure of hexagonal $Ba_3Ti_2RuO_9$.

The parent structure for $Ba_3Ti_2RuO_9$ is hexagonal $BaTiO_3$, which has the space group $P6_3/mmc$. The structural phases accessible to $BaTiO_3$ are shown in Fig. 1.

The three phases between 183 and 393 K, which are separated by displasive phase transitions, are ferroelectric, whilst the cubic and high-temperature hexagonal phase above 1703 K is non-ferroelectric.

The hexagonal polymorph of $BaTiO_3$ was first reported by Megaw (1946). Subsequently it was established (Burbank & Evans, 1948) that it has a six-layer (6H) structure built up of six close-packed layers of BaO_3. In contrast to the cubic form, which has *ABC* stacking, the 6H form has the stacking sequence *ABCACB* and the unit cell contains six formula units of $BaTiO_3$. Each of the six Ti atoms in the structure is located in a cage of six O atoms, which form a TiO_6 octahedron. These six sites are subdivided into two crystallographically inequivalent positions. The twofold Ti positions are located in corner-sharing octahedra, while the fourfold positions are located in Ti_2O_9 coordination groups (pairs of TiO_6 octahedra that share an octahedral face). A diagram of the hexagonal structure is given in Fig. 2.

The lattice parameters for the pure 6H hexagonal phase of $BaTiO_3$ were refined in a single-crystal X-ray study at 296 K as: $a = 5.7238$, $c = 13.9649$ Å (Akimoto *et al.*, 1994).

Perfect crystals of hexagonal $BaTiO_3$ are extremely difficult to stabilize at room temperature, however, metastable preparations have been achieved, under reducing conditions, by cooling rapidly (10 K min^{-1}) from the cubic to hexagonal transition temperature (Eibl & Skalicky, 1989).

In $Ba_3Ti_2RuO_9$, the partial substitution of Ti atoms with Ru stabilizes the hexagonal phase at room temperature. The mechanism for this will depend upon the location of the Ru atom in the structure. It has been assumed that Ru substitutes for Ti on half of its fourfold sites so there is one substitution cation per Ti_2O_9 coordination group in the unit cell. If this is the case, the interaction between the dopant atom with its neighbouring Ti atom will drive the formation of the hexagonal structure. Face-sharing coordination between octahedra becomes energetically favourable over corner-sharing because of the overlap of *d* electrons between the face-shared octahedra (Dickson *et al.*, 1961). Whilst this scenario is chemically plausible, the atomic site, sequence and degree of ordering of the Ru atoms has not been measured directly, nor has the space group been established. In the present work, convergent-beam electron diffraction has been used to determine the space group and hence the site and sequence of the Ru atoms in the unit cell. In addition, high-resolution electron microscopy has been used to examine microstructures generated by the Ru substitution.

2. Experimental

Microcrystalline titanium oxide was prepared by the hydrolysis of a 2-propanol solution of titanium isopropoxide, $Ti(OPr^i)_4$. The dried powder was intimately mixed with stoichiometric quantities of $BaCO_3$ and RuO_2 and fired in an alumina boat in air for 24 h at 1263 K. This gave a microcrystalline product of stoichiometry $Ba_3Ti_2RuO_9$. Crystals were grown from this powder according to the method of Blattner *et al.* (1947), by heating in molten $BaCl_2$ in an alumina crucible in a tube furnace. After 72 h most of the barium chloride had evaporated and hexagonal crystal plates with basal faces up to 2 mm and of thickness less than 0.1 mm were easily separated from the remaining solidified flux by washing with water.

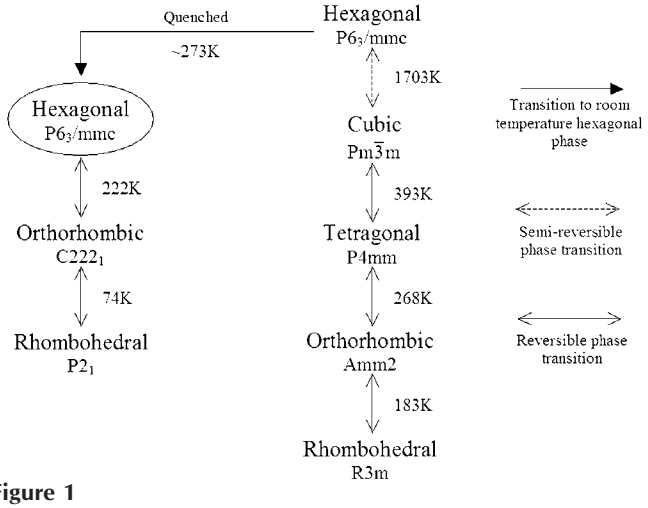

Figure 1
Transition temperatures of phase transitions in barium titanate (Tanaka *et al.*, 2002; Harada *et al.*, 1970; Shirane *et al.*, 1957; Hewat, 1974).

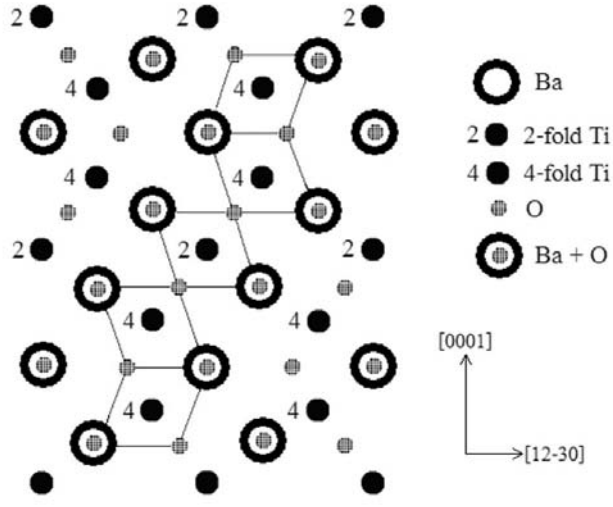

Figure 2
Hexagonal structure of $BaTiO_3$ projected along $[10\bar{1}0]$ indicating two- and fourfold Ti sites and Ti_2O_9 coordination groups.

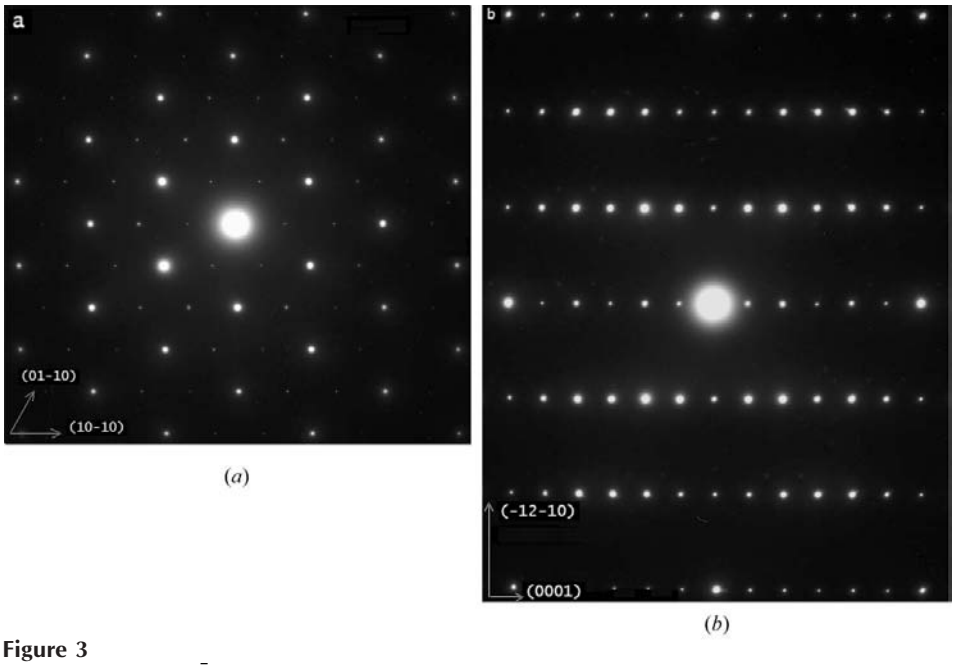

Figure 3
(*a*) [0001] and (*b*) [10$\bar{1}$0] SAED patterns of $Ba_3Ti_2RuO_9$ consistent with a hexagonal unit cell with h.c.c. stacking.

A single crystal was lightly crushed under ethanol and cleaved fragments were allowed to settle onto a holey carbon copper grid. The grid was then placed in an oven at 353 K to complete the evaporation of the ethanol.

The specimens were examined using a LaB_6 200 kV Jeol 2011 transmission electron microscope fitted with an analytical pole piece and a LaB_6 400 kV Jeol 4000EX transmission electron microscope fitted with a high-resolution pole piece. Selected-area, convergent-beam and large-angle convergent-beam electron diffraction patterns, and high-resolution electron microscope images were taken to establish the stacking sequence, space group and microstructure. Energy-dispersive X-ray spectra were taken to confirm the stoichiometry. Crystals were found to be stable under all of these experimental conditions.

3. Results and discussion

3.1. Structure determination

Selected-area electron diffraction (SAED) patterns taken along the [0001] (Fig. 3*a*) and [10$\bar{1}$0] (Fig. 3*b*) zone axes are consistent with a hexagonal 6H unit cell. This is consistent with the h.c.c. structure of hexagonal $BaTiO_3$ (Fig. 2; Akimoto *et al.*, 1994). Dickson *et al.* (1961) proposed the same stacking sequence of BaO_3 layers for $Ba_3Ti_2RuO_9$ with the Ru atoms partially occupying the fourfold octahedral sites. The relative positions and degree of order of the Ru and Ti atoms on these sites will determine the space group. In this section we determine the space group and hence determine the sequence of Ru and Ti atoms on the fourfold sites in the *c*-axis direction.

Convergent-beam electron diffraction (CBED) can uniquely determine 218 of the 230 space groups (Goodman, 2001). We took CBED patterns along the [0001] and [10$\bar{1}$0] zone axes and these proved to be sufficient to determine the space group uniquely as follows.

3.1.1. Point group. The whole pattern symmetry of the [0001] CBED pattern (Fig. 4*a*) is 6*mm*, which is consistent (Buxton *et al.*, 1976) with the point groups 6*mm* or 6/*mmm* (Table 1). The whole pattern symmetry of the [10$\bar{1}$0] CBED pattern is *m*, whilst the bright-field symmetry and the higher-order Laue zone (HOLZ) symmetry are 2*mm* (Fig. 4*b*), which is consistent with the six possible point groups in Table 1.

Taken together, it is evident that the only point group consistent with both zone-axis pattern symmetries is 6*mm*.

We emphasize that the observation differentiating between point group 6*mm* and 6/*mmm* is subtle. It is most evident in small differences in the intensity distribution between certain pairs of 00*l* and 00$\bar{l}$*Z* (*l* even) reflections in the [10$\bar{1}$0] CBED pattern. Although this is a small effect, it was consistently observed in all of the [10$\bar{1}$0] patterns we recorded, taken from several different crystals with a variety of thicknesses. We note that the pattern is aligned precisely along the zone axis, as confirmed by the perfect 2*mm* symmetry of the HOLZ lines and of some pairs of zero-order reflections. We are therefore confident that this is an effect due to the unit-cell symmetry and not induced by specimen shape, tilt or defects. However, because the effect is so weak, we sought to find further evidence by comparing conjugate reflection pairs, g and $\bar{g}$ (Goodman & Lehmpfuhl, 1968; Goodman, 1975, 2001), as follows.

Pairs of CBED patterns were also taken near the [10$\bar{1}$0] zone axis, one placing the 002 reflection close to the Bragg condition and the other the 00$\bar{2}$ reflection (Fig. 5). A striking difference between the intensity distribution between the two patterns can be observed in the overlap of the 012/013 (in Fig. 5*a*) and 01$\bar{2}$/01$\bar{3}$ (in Fig. 5*b*) reflections (lower arrow) and 0$\bar{1}$2/0$\bar{1}$3 (in Fig. 5*a*) and 0$\bar{1}\bar{2}$/0$\bar{1}\bar{3}$ (in Fig. 5*b*) reflections (upper arrow), whereas in the overlap of the 01$\bar{4}$/01$\bar{5}$ (in Fig. 5*a*) and 014/015 (in Fig. 5*b*) reflections (upper arrow) and 0$\bar{1}\bar{4}$/0$\bar{1}\bar{5}$ (in Fig. 5*a*) and 0$\bar{1}$4/0$\bar{1}$5 (in Fig. 5*b*) reflections (lower arrow), the intensity distribution is identical. In addition, there is a slight difference between the 002 and 00$\bar{2}$ reflections which is difficult to identify in the reproduction. This experiment provides definitive evidence of the lack of a centre of symmetry.

We note that the CBED patterns in some of the above experiments were recorded using high dynamic-range image

Table 1
Possible diffraction and point groups.

Orientation	Diffraction group	Possible point groups
[001]	$6mm$	$6mm$
	$6mm1_R$	$6/mmm$
[100]	$m1_R$	$mm2$
		$4mm$
		$\bar{4}2m$
		$6mm$
		$6m2$
		$\bar{4}3m$

plates to ensure that all parts of the pattern symmetry could be measured simultaneously. Initially we had tried photographic film but found its very limited dynamic range made it extremely difficult to be confident of the whole pattern symmetry. Table 1 lists the possible diffraction groups and their corresponding point groups (Buxton *et al.*, 1976).

3.1.2. Space group. Gjønnes–Moodie (G–M) extinction lines (Gjønnes & Moodie, 1965) are observed parallel to [0001] in the odd-order reflections, indicating the presence of a glide line parallel to **c**. Of the space groups with point-group symmetry $6mm$ (namely, $P6mm$, $P6cc$, $P6_3cm$ and $P6_3mc$), only $P6_3mc$ contains the *c*-glide symmetry. Thus, the space group of $Ba_3Ti_2RuO_9$ is $P6_3mc$ (186), which is a reduction in symmetry from the space group $P6_3/mmc$ (194) of pure hexagonal $BaTiO_3$ (Burbank & Evans, 1948). The symmetry is lowered by the loss of a mirror plane perpendicular to the *c* axis and is seen explicitly in the $[10\bar{1}0]$ CBED pattern symmetry (Fig. 4*b*). The loss of the mirror but retention of the *c* glide uniquely defines the arrangement of the Ru and Ti atoms on the fourfold sites (Fig. 6). In order to break the mirror plane and preserve the glide plane, the Ru and Ti atoms must alternate on the fourfold sites.

The above experiments were repeated using a liquid nitrogen cooling holder to cool the specimen to a *nominal* 110 K. The space group was found to be the same, $P6_3mc$.

3.2. Lattice parameter determination

We measured the lattice parameters of $Ba_3Ti_2RuO_9$ with powder X-ray diffraction on a Bruker D8 X-ray diffractometer. Cu $K\alpha$ radiation was used with a 2θ scan range of 2–92° at room temperature. The computer program *CELSIZ* in conjunction with reference traces in the ICDD-JCPDS Powder Diffraction FILE database were employed to refine the unit-cell length. *CELSIZ* corrected the standard line positions for each analysis and then used a least-squares fitting procedure of measured and calculated peak centroids for a number of peaks in the X-ray patterns to calculate the lattice dimensions and their standard deviations. The refined lattice parameters are $a = 5.7056 \pm 0.0005$, $c = 14.0093 \pm 0.0015$ Å. This is comparable to the lattice parameters for $BaTiO_3$ from X-ray single-crystal measurements given above (Akimoto *et al.*, 1994).

3.3. Microstructure

Microstructure was examined using high-resolution electron microscopy, selected-area and convergent-beam electron diffraction.

The most common microstructural defect was observed in [0001] HREM images as a low strain, highly coherent grain boundary aligned approximately parallel to the $(10\bar{1}0)$ planes and hence intersecting at 60 and 120° (Fig. 7*a*). The misorientation between adjacent grains was measured using CBED and found to be less than 1°. Furthermore, no difference could be detected between the [0001] zone-axis CBED patterns from adjacent grains. This suggests that the only difference

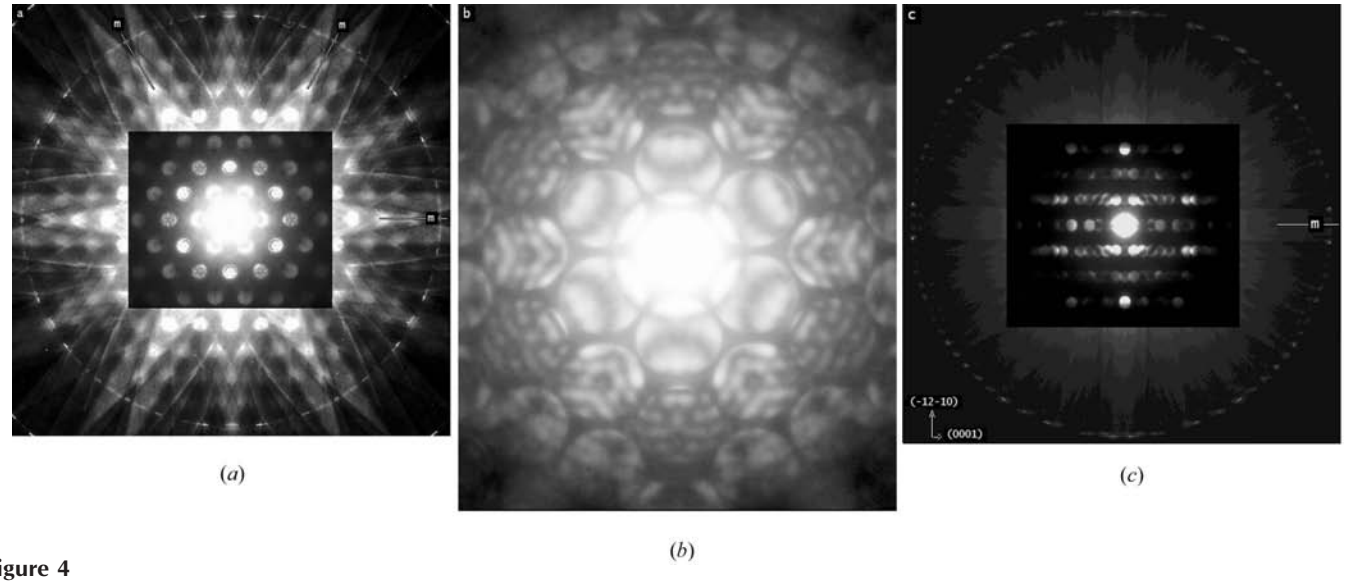

Figure 4
(*a*), (*b*) [0001] CBED patterns of $Ba_3Ti_2RuO_9$ with $6mm$ symmetry. (*b*) Taken with almost twice the convergence angle of (*a*) and a lower exposure time, highlights the $6mm$ symmetry of the inner reflections. (*c*) $[10\bar{1}0]$ CBED pattern of $Ba_3Ti_2RuO_9$ with a mirror plane perpendicular to **a*** but no mirror plane perpendicular to **c*** (compare for example the 006 and $00\bar{6}$ reflections). The $2mm$ symmetry of the HOLZ confirms the zone axis is aligned precisely. For clarity, the HOLZ are displayed in (*a*) and (*c*) using a different intensity scale to the ZOLZ.

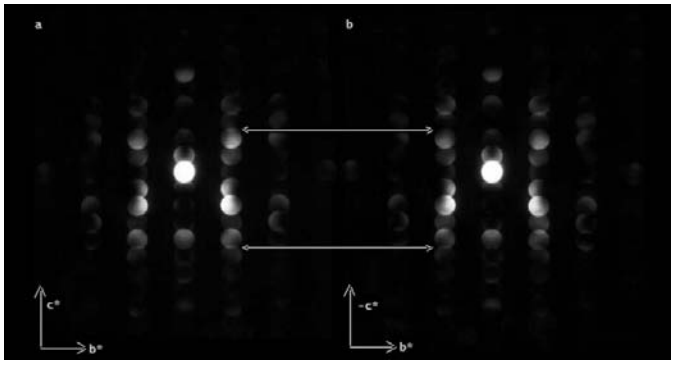

Figure 5
Comparison of conjugate pairs: CBED patterns of $Ba_3Ti_2RuO_9$ taken with (*a*) 002 and (*b*) $00\bar{2}$ close to the Bragg angle. Differences in the intensity distribution are most visible in overlap of the 012/013 and $01\bar{2}/01\bar{3}$ reflections. See arrows.

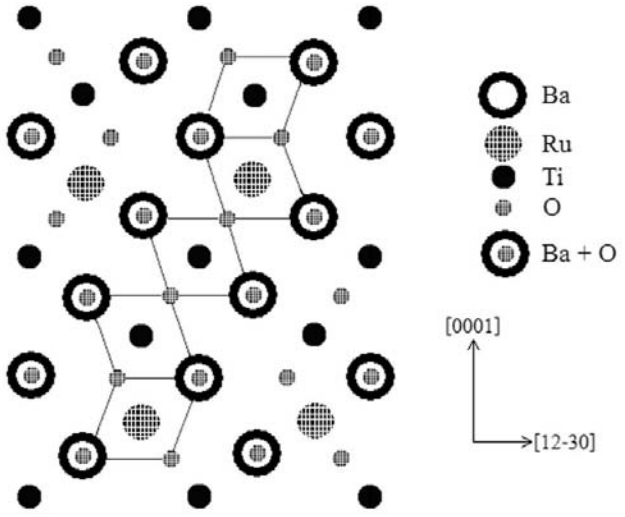

Figure 6
Schematic of the structure of $Ba_3Ti_2RuO_9$ in the $[10\bar{1}0]$ projection indicating the alternate Ru and Ti atom positions which are uniquely defined by the space-group symmetry.

between adjacent grains may be the order in which the Ru and Ti atoms are stacked along the *c* axis (Fig. 7*c*). In other words, they are effectively anti-phase boundaries, with one grain aligned parallel to [0001] and its neighbour aligned parallel to $[000\bar{1}]$. In principal, this should generate a very small difference in the intensity of HOLZ lines between the two patterns. Dynamical calculations of the CBED patterns generated by phase 1 and phase 2 suggest this difference is too small to be detected experimentally and this is consistent with our observations.

We also often observe that 'pairs' of antiphase boundaries often meet (as in Fig. 7*a*), with a narrow channel, a few atoms wide, separating domains of the same phase. This suggests that the formation of these interfaces is not random but may be governed by a long-range force. We speculate wildly as to whether this force might be associated with an electric polarization and/or a tilting of the octahedra induced by the Ru substitution.

The presence of such boundaries should be taken into account in the interpretation of any electronic measurements made on this material.

In addition to these antiphase boundaries, stacking faults were occasionally observed, both directly in $[10\bar{1}0]$ HREM images and as weak streaks of intensity along the *c* axis in the corresponding selected-area diffraction patterns.

4. Conclusions

We have determined the space group of hexagonal $Ba_3Ti_2RuO_9$ to be the non-centrosymmetric $P6_3mc$. The Ru atoms are located on the fourfold sites, alternating with Ti along the *c*-axis. The presence of the Ru atoms on these sites drives the formation of the hexagonal structure because face-sharing octahedra, with their overlapping *d*-electrons, are energetically favoured over a corner-sharing configuration.

We have measured the lattice parameters using X-ray powder diffraction to be $a = 5.7056 \pm 0.0005$, $c = 14.0093 \pm 0.0015$ Å at room temperature.

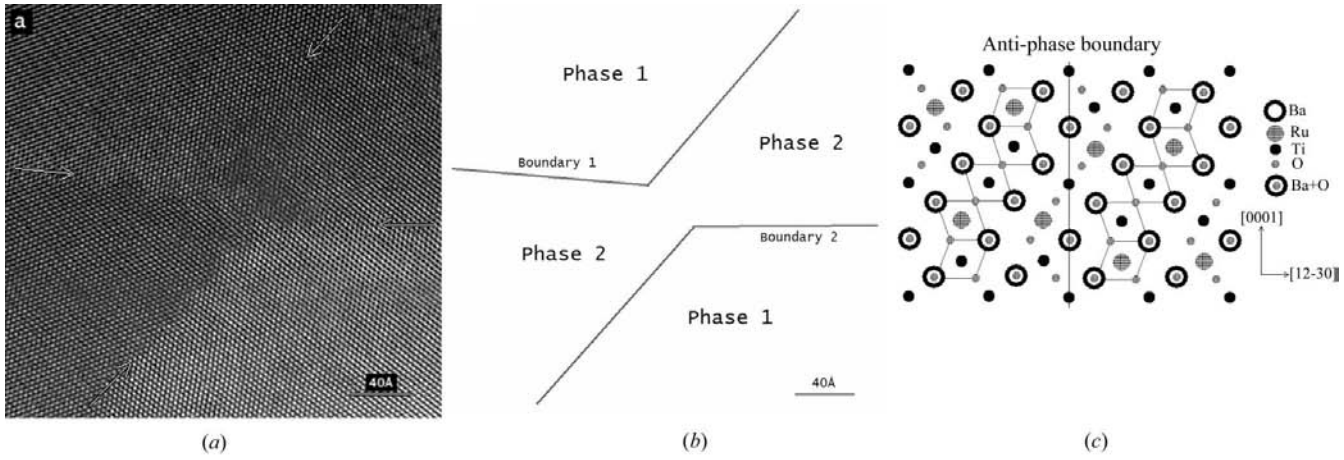

Figure 7
(*a*) HREM image of two pairs of anti-phase boundaries in a large flat hexad of $Ba_3Ti_2RuO_9$. (*b*) Schematic of boundaries visible in (*a*). (*c*) Schematic of antiphase boundary indicating the swap in Ru, Ti ordering.

We observed {100} grain boundaries which we attribute to being the interface between crystals of opposite polarity in the ⟨0001⟩ direction. That is, the Ru and Ti sequence is reversed across the boundary. Further we observe that pairs of such boundaries often meet in an intriguing configuration that suggests their growth may be governed by long-range force(s).

We acknowledge useful discussions with C. J. Rossouw. CJM thanks the Australian Research Council for an Australian Postgraduate Award and the CSIRO for a postgraduate top-up scholarship. This work was facilitated by the Australian Research Council infrastructure grant LE0238381.

References

Akimoto, J., Gotoh, Y. & Oosawa, Y. (1994). *Acta Cryst.* C**50**, 160–161.
Blattner, H., Matthias, B. & Merz, W. (1947). *Helv. Phys. Acta*, **20**, 225–228.
Burbank, R. D. & Evans, H. T. (1948). *Acta Cryst.* **1**, 330–336.
Buxton, B. F., Eades, J. A., Steeds, J. W. & Rackham, G.M. (1976). *Philos. Trans. R. Soc. London*, **181**, 171–193.
Dickson, J. G., Katz, L. & Ward, R. (1961). *J. Am. Chem. Soc.* **83**, 3026–3029.
Eibl, O. & Skalicky, P. (1989). *Philos. Mag.* **60**, 601–612.
Gjønnes, J. K. & Moodie, A. F. (1965). *Acta Cryst.* **19**, 65–67.
Goodman, P. (1975). *Acta Cryst.* A**31**, 804–810.
Goodman, P. (2001). *International Tables for Crystallography*, Vol. B, pp. 285–306. Dordrecht: Kluwer Academic Publishers.
Goodman, P. & Lehmpfuhl, G. (1968). *Acta Cryst.* A**24**, 339–347.
Grey, I. E., Li, C., Cranswick, L. M. D., Roth, R. S. & Vanderah, T. A. (1998). *J. Solid State Chem.* **135**, 312–321.
Hill, N. A. (2000). *J. Phys. Chem. B*, **104**, 6694–6709.
Harada, J., Axe, J. D. & Shirane, G. (1970). *Acta Cryst.* A**26**, 608–612.
Hewat, A. W. (1974). *Ferroelectrics*, **6**, 215–218.
Keith, G. M., Rampling, M. J., Sarma, K., Alford, N. M. & Sinclair, D. C. (2004). *J. Eur. Ceram. Soc.* **24**, 1721–1724.
Langhammer, H. T., Müller, T., Felgner, K. H. & Abicht, H. P. (2000). *J. Am. Ceram. Soc.* **83**, 605–611.
Megaw, H. D. (1946). *Proc. Phys. Soc.* **58**, 133–152.
Shirane, G., Danner, H. & Pepinsky, R. (1957). *Phys. Rev.* **105**, 856–860.
Tanaka, M., Terauchi, M. & Tsuda, K. (2002). *Convergent Beam Electron Diffraction*, Vol. IV, pp. 124–131. Japan: Jeol Ltd.